Discrete-Impedance Metasurfaces for Wireless Communications in D-Band

Sergei Kosulnikov, Xuchen Wang, and Sergei A. Tretyakov, *Fellow, IEEE*

***Abstract*— Engineering and optimization of wireless propagation channels will be one of the key elements of future communication technologies. Metasurfaces may offer a wide spectrum of functionalities for passive and tunable reflecting devices, overcoming fundamental limits of commonly used conventional phase-gradient reflectarrays and metasurfaces. In this article, we develop an efficient way for the design and implementation of metasurfaces with high-efficiency anomalous reflector functionalities. The developed numerical method provides accurate, fast, and simple metasurface designs, taking into account nonlocal near-field interactions between array elements. The design method is validated by manufacturing and experimental testing of highly efficient anomalous reflectors for the millimeter-waveband.**

***Index Terms*— Diffraction grating, far-field scattering, metasurface, reflection coefficient.**

I. Introduction

NOVEL wireless communication technologies are targeted for the need of growing data transfer rates, which leads to a shift to higher operational frequencies. The millimeter-wave (MM-wave) technologies become a basis for new generations of the wireless communication systems. However, communications at such high frequencies suffer from high free-space attenuation even in indoor scenarios. For this reason, it is necessary to use highly directive antennas, losing the advantages of multipath propagation that usually provides connectivity even without a direct line of sight (LOS) between the antennas. One of the very noticeable techniques potentially solving this issue is based not on modifications of the source and/or receiver itself, but on modifications and optimizations of the propagation environment. Indeed, especially indoors, it is very attractive to realize a scenario where the signal will be efficiently relayed from some off-site objects. It is worth noting that repeater-like-devices do not have to be active: even a passive but smart optimization of the signal propagation path can improve the communication channel by reflecting or transmitting wave beams toward the desired directions. We also note that this approach is in line with the "green trends" for efficient and ecological resource utilization. In this work, we consider a particular example of passive anomalous reflectors that reflect incident waves to arbitrarily set reflection angles. This functionality can be used to create an effective wireless link for nonline-of-sight (NLOS) communications even for MM-wave systems based on the use of high-gain antennas. Fig. 1 illustrates the considered scenario, where the signal from the transmitter cannot reach the receiver in the LOS mode due to a wall obstacle, but still a reliable wireless channel is set due to redirecting and focusing the reflected signal by an anomalously reflecting metasurface.

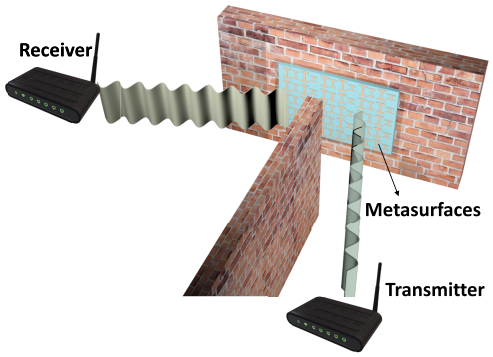

Fig. 1. Application scenario of an anomalous reflector in MM-wave wireless communications.

The research of anomalous reflectors has been actively going on from 60's. Perhaps the earliest anomalous reflectors are reflectarrays where each element separated by $\lambda/2$ distance from neighboring elements locally reflects at different phases, forming a desired reflection wavefront [1], [2]. However, for grazing reflection angles, the device efficiency significantly drops. Later, this idea was implanted in arrays with subwavelength unit cells: phase-gradient metasurfaces [3], [4]. The reflection phase of each unit cell of the metasurface (realized as a periodical lattice of cells) is linearly and periodically varying on the surface. Still, such phase-gradient metasurfaces inherit the main drawbacks of reflectarrays: high reflection efficiency is achievable only when the deviation from the usual reflection law is not large. At sharp reflection angles, spurious scattering dramatically increases. Since 2016, it is recognized that low efficiency of a device operating far from the specular or retroreflection regimes is caused mainly by the impedance mismatch of the incident and reflected waves [5], [6]. For a given plane-wave incidence, considering only a single-plane wave reflection, it is not enough to satisfy the local lossless boundary condition of the metasurface [6]. In [7], it was pointed out that evanescent fields have to be engaged and optimized to realize a purely reactive boundary that perfectly directs an incident plane wave to an anomalous

This work was supported in part by the European Commission through the Horizon 2020 Artificial Intelligence Aided D-band Network for 5G Long Term Evolution (ARIADNE) project under Grant 871464 and in part by the Academy of Finland under Grant 345178.*(Corresponding author: Xuchen Wang.)*

Sergei Kosulnikov and Sergei A. Tretyakov are with the Department of Electronics and Nanoengineering, Aalto University, 00079 Aalto, Finland (e-mail: sergei.2.kosulnikov@aalto.fi; sergei.tretyakov@aalto.fi).

Xuchen Wang is with the Institute of Nanotechnology, Karlsruhe Institute of Technology, 76131 Karlsruhe, Germany (e-mail: xuchen.wang@kit.edu).

direction. Based on this general principle, different design methods have been proposed. For example, in [8] and [9], the evanescent fields are optimized by ensuring local power conservation on the surface and finding a locally reactive surface. In contrast, the design methods in [10], [11] and [12] are based on the global power conservation, where the structures of meta-atoms are collectively optimized within a supercell. This method was recently used for the creation of anomalous reflectors in D-band [13], where patch sizes in a supercell were collectively optimized starting from the local periodic approximation as an initial guess, with good results. In parallel, the meta-grating method [14], [15] was suggested as another alternative to realize perfect anomalous reflection with a reduced number of meta-atoms.

In this article, we propose an effective design method for the realization of perfect anomalous reflection into arbitrary directions. As a basis for design, we select an impedance sheet placed on a grounded dielectric substrate. We first discretize the impedance sheet into finite elements with uniform values of the sheet reactance. For this discretized structure, we derive an analytical formula for all the scattered Floquet modes of the metasurface. Then, we use an inverse design optimization method to optimize the discrete impedances until the amplitudes (and possibly phases) of the scattered modes satisfy the design objectives. This method is different from the known impedance-based methods [8], [16], where the sheet impedance is first assumed to be continuous in the optimization process and discretized into finite elements only after optimization. After discretization, such metasurfaces may not behave as perfect as expected from the theoretical results of the continuous-profile optimization. In contrast, in the proposed method, the sheet impedance is optimized already in the discretized form. Therefore, the performance does not suffer from degradations caused by surface discretization. In addition, the proposed method is not limited by the requirement of the local power conservation on the surface: the input impedance seen at the input surface can take purely imaginary or complex values. The overall passivity of the device is automatically ensured due to the passivity of the impedance sheet and the substrate material. Therefore, the optimized results encompass both realization possibilities (local or global power conservation), which is more general than in the earlier developed methods. In addition, using the same approach, it is possible to design other devices for wave shaping, such as multichannel beam splitters with arbitrarily assigned power ratios.

This article is organized as follows. In Section II, we introduce the theoretical model of the developed numerical optimization method; in Section III, we focus on a particular example implementing an anomalous reflector operating at D-band; Section IV is focused on the experimental validation of the implemented anomalous reflector; Section V shows benefits of the suggested design method comparing to the conventional approach; the conclusions and discussion section is closing this article.

II. Discrete Sheet Impedance Model for Reflection Optimization

In the sheet-impedance model, the metasurface is assumed to be formed by an impedance sheet on top of a grounded

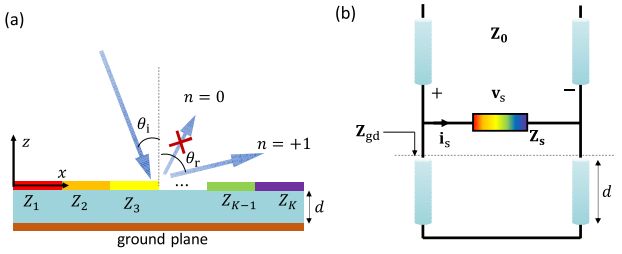

Fig. 2. (a) Side view of a metasurface containing discrete impedance sheets on a grounded substrate. (b) Equivalent circuit of the metasurface.

dielectric substrate with permittivity $\epsilon_{\rm d}$ and thickness d. The sheet is characterized by the nonuniform sheet impedance $Z_{\rm s}$ that relates the tangential component of the macroscopic electric field and the surface current density flowing on the sheet. Fig. 2(a) shows a single unit cell of the metasurface with the spatial periodicity D (the size of one supercell). In earlier work [17], the impedance distribution $Z_{\rm s}(x)$ was assumed to be a continuous function of the tangential coordinates. The impedance distribution was optimized to achieve the desired performance, and next discretized into a number of uniform-impedance strips (subcells) to allow practical realizations as arrays of properly shaped patches. However, discretization of the optimal continuous distribution leads to some deterioration of performance. Here, we improve the design method by initially optimizing piecewise uniform-impedance sheets, corresponding to discrete sets of meta-atoms. In this way, we avoid performance degradation caused by discretization errors.

We discrete one supercell into K elements, as shown in Fig. 2(a), where the central coordinate of the kth cell is denoted as $x_k = (2k-1)D/2K$. The sheet impedance of the kth subcell is denoted as Z_k, where $k \in [1, K]$. The discretized sheet impedance profile $Z_{\rm s}(x)$ is piecewise homogeneous and can be viewed as a cascade of K step functions. As for any periodic function, it can be decomposed into Fourier series as follows:

$$Z_{\rm s}(x) = \sum_{m=-\infty}^{+\infty} g_m e^{-jm\beta_{\rm M}x} \tag{1}$$

where g_m is the Fourier coefficient. A plane wave illuminates the metasurface at the angle of $\theta = \theta_{\rm i}$. Due to the periodicity of the reflector, the scattered field is a sum of an infinite number of Floquet harmonics, denoted by index n. The tangential wavevector of the Floquet modes scattered from periodical structures can be written as $k_{xn} = k_0 \sin\theta_{\rm i} + n\beta_{\rm M}$, where $\beta_{\rm M} = 2\pi/D$ is the spatial modulation frequency of the surface impedance, n is the mode order, $\theta_{\rm i}$ is the incident angle, and $k_0 = \omega_0\sqrt{\epsilon_0\mu_0}$ (ω_0 is the incident-wave frequency) is the free-space wavenumber. Modes satisfying $|k_{xn}| < k_0$ propagate into the far-zone at the angles θ_n, defined by

$$\sin\theta_n = \frac{k_0 \sin\theta_{\rm i} + n\beta_{\rm M}}{k_0}. \tag{2}$$

For $|k_{xn}| > k_0$, the modes are evanescent, exponentially decaying along the surface normal. Next, based on the *mode-matching* method, we aim to find the amplitudes of all

scattered modes at the metasurface plane ($z = 0$). For convenience of analysis, we use the transmission-line model shown in Fig. 2(b). The sheet impedance is modeled as a shunt impedance in the transmission line. The grounded substrate is modeled as a shorted transmission line with its length equal to the substrate thickness. The current and voltage in the transmission-line model are analogous to the total tangential magnetic and electric fields on the surface ($z = 0$). Unlike conventional transmission-line modeling of uniform metasurfaces, where the current and voltage only have one mode and can be treated as scalar numbers, in this case, the space-modulated metasurface excites infinitely many spatial modes (including propagating and evanescent ones). Therefore, the current and voltage in the transmission line are not simple scalar numbers but infinite sums

$$I_s(x) = \sum_{n=-\infty}^{+\infty} i_s^n e^{-jk_{xn}x} \tag{3a}$$

and

$$V_s(x) = \sum_{n=-\infty}^{+\infty} v_s^n e^{-jk_{xn}x}. \tag{3b}$$

The current and voltage on the impedance sheet must obey Ohm's law, $V_s(x) = Z_s(x)I_s(x)$. Substituting (3a), (3b), and (1) into Ohm's law, we have

$$\sum_{n=-\infty}^{+\infty} v_s^n e^{-jk_{xn}x} = \sum_{n=-\infty}^{+\infty}\sum_{m=-\infty}^{+\infty} g_m i_s^n e^{-jk_{x,n+m}x}. \tag{4}$$

By shifting the summation order n to n–m on the right side of (4), we get an expression where both sides share the same basis $e^{-jk_{xn}x}$, which can be eliminated together with the summation over n. Therefore, (4) can be simplified as follows:

$$v_s^n = \sum_{m=-\infty}^{+\infty} g_m i_s^{n-m}. \tag{5}$$

One can see from (5) that every voltage harmonic is related to all current harmonics due to mode coupling. Considering a finite number of Floquet modes from $n = -N$ to $n = N$, (5) can be written in a form of matrix multiplication

$$\begin{pmatrix} v_s^{-N} \\ v_s^{1-N} \\ \vdots \\ v_s^{+N} \end{pmatrix} = \begin{pmatrix} g_0 & g_{-1} & \cdots & g_{-2N} \\ g_1 & g_0 & \cdots & g_{1-2N} \\ \vdots & \vdots & \ddots & \vdots \\ g_{2N} & g_{2N-1} & \cdots & g_0 \end{pmatrix} \begin{pmatrix} i_s^{-N} \\ i_s^{1-N} \\ \vdots \\ i_s^{+N} \end{pmatrix}. \tag{6}$$

Denoting the voltage and current arrays in (6) as $\mathbf{v}_s$ and $\mathbf{i}_s$, and the $(2N+1)$ dimensional impedance matrix as $\mathbf{Z}_s$, (6) can be written in a simple form: $\mathbf{v}_s = \mathbf{Z}_s \cdot \mathbf{i}_s$. The impedance matrix accounts for mutual coupling between different modes. This is a powerful and convenient method extensively utilized in studies of diverse physical systems, including circuits [18], communication systems [19], and electromagnetic systems [15], [20].

Similar to the sheet impedance, the input impedance of the grounded substrate can also be written in matrix form. Since the substrate is spatially uniform and there is no mode coupling in the uniform substrate, the impedance of the grounded substrate is a $(2N+1)$ dimensional *diagonal* matrix $\mathbf{Z}_{gs}$. The nth diagonal term is the input impedance of grounded substrate for the nth scattering mode (note that we number the matrix columns and rows from $-N$ to $+N$ instead of from 1 to $2N+1$)

$$\mathbf{Z}_{gs}(n,n) = \frac{1}{Z_{d,n}\tanh(jk_{zn}^d d)}. \tag{7}$$

Here, $Z_{d,n}$ is the wave impedance of the dielectric substrate material, and $k_{zn}^d = \sqrt{\omega_0^2\epsilon_0\epsilon_d\mu_0 - k_{xn}^2}$ is the normal component of the wavevector in the dielectric substrate for the nth mode. For TE-polarized waves, $Z_{d,n} = (\mu_0\omega_0)/k_{zn}^d$, and for TM polarized waves, $Z_{d,n} = k_{zn}^d/(\omega_0\epsilon_0\epsilon_d)$. Details for derivation of (7) can be found in Section IV of the Supplementary Material of [16].

The total input impedance of the metal-backed metasurface can be calculated as a parallel connection of the gradient penetrable impedance (characterized by $\mathbf{Z}_s$) of the sheet and the input impedance of the metal-backed substrate $\mathbf{Z}_{gs}$, that is, $\mathbf{Z}_{tot} = \mathbf{Z}_s||\mathbf{Z}_{gs}$. After $\mathbf{Z}_{tot}$ is determined, we can calculate all the scattered modes for a given incidence in terms of a reflection matrix. The reflection matrix is defined as follows:

$$\mathbf{\Gamma}_{TM} = (\mathbf{Z}_{tot} + \mathbf{Z}_0)^{-1} \cdot (\mathbf{Z}_0 - \mathbf{Z}_{tot}) \tag{8}$$

for TM-polarized incidence. Here, $\mathbf{Z}_0$ is the wave impedance of free space, which is a diagonal matrix. The nth element of $\mathbf{Z}_0$ has the same format with $Z_{d,n}$, only assuming $\epsilon_d = 1$. The reflection matrix for TE-polarized incidence is as follows:

$$\mathbf{\Gamma}_{TE} = (\mathbf{Y}_{tot} + \mathbf{Y}_0)^{-1} \cdot (\mathbf{Y}_0 - \mathbf{Y}_{tot}) \tag{9}$$

where $\mathbf{Y}_{tot} = \mathbf{Z}_{tot}^{-1}$ and $\mathbf{Y}_0 = \mathbf{Z}_0^{-1}$ are the admittance matrices. The derivation details of (8) and (9) are presented in Appendix. The reflection matrix relates the *tangential* components of the incident and reflected fields, that is, $\mathbf{E}_r = \mathbf{\Gamma}_{TE}\cdot\mathbf{E}_i$ for TE waves and $\mathbf{H}_r = \mathbf{\Gamma}_{TM} \cdot \mathbf{H}_i$ for TM waves. The incident and reflected tangential fields ($\mathbf{E}_i$, $\mathbf{E}_r$, $\mathbf{H}_i$, and $\mathbf{H}_r$) should be represented by $2N+1$-dimensional vertical vectors. The vector contains the complex amplitudes of the considered harmonics.

The above theory shows how to calculate all the scattered harmonics for a given set of discrete impedance sheets and illumination waves. However, the design of metasurfaces is an inverse problem: for a given incidence and desired reflection harmonics, how to find a proper set of discrete impedance values? Since there is no analytical solution for this inverse problem, we use mathematical optimization. Next, we introduce the optimization principles. For a single TE-polarized plane-wave incidence, $\mathbf{E}_i$ can be written as follows:

$$\mathbf{E}_i = [0, \ldots, 0, 1, 0, \ldots, 0]^T \tag{10}$$

where the incident mode ($n = 0$) is positioned in the middle of the array. For a known illumination (a given $\mathbf{E}_i$), our goal is to find a proper set of discrete grid impedances of an array that realizes the desired $\mathbf{E}_r$. Here, we focus on the perfect anomalous reflection functionality with the incident power fully reflected to the $n = +1$ scattering order. Therefore, the desired reflected field vector can be written as follows:

$$\mathbf{E}_r = [0, \ldots, 0, 0, A_{obj}, \ldots, 0]^T \tag{11}$$

where $A_{\text{obj}} = \sqrt{\cos\theta_{\text{i}}/\cos\theta_{\text{r}}}$ is the amplitude of reflection that ensures that all the incident power is directed to the anomalous direction [6]. This goal is realized by optimizing the discrete impedance values $Z_1, Z_2, \ldots, Z_K$ (purely reactive), or, equivalently to say, optimizing the reflection matrix $\mathbf{\Gamma}_{\text{TE}}$, until the desired reflection mode amplitude is maximized in the reflection vector $\mathbf{E}_{\text{r}}$. Here, we use the mathematical optimization tool available in the MATLAB package to find the optimal values of the impedance sheets. In each trial of the optimization, MATLAB assumes an array of $Z_1, Z_2, \ldots, Z_K$ and calculates the reflected fields. Denoting the calculated amplitude of the desired reflection mode in each trial as A_{cal}, the optimization goal is to find a proper set of $Z_1, Z_2, \ldots, Z_K$ that minimizes the cost function defined as follows:

$$F(Z_1, Z_2, \ldots, Z_K) = |A_{\text{cal}} - A_{\text{obj}}|. \tag{12}$$

Employing the MultiStart and $fmincon$ algorithms, MATLAB can search for the minimum value of F in the multidimensional parameter space. In the examples presented here, the optimization time with the described method was in the order of tens of minutes using a usual desktop computer (Intel-i5-based CPU with 32 Gb RAM).

It is important to mention that this approach is quite general. It can be used for the design of Floquet metasurfaces with arbitrary power distributions among all the possible Floquet modes, for example, beam splitters, only by modifying the objective function in (12). In addition, the desired reflection phases can also be set arbitrarily.

III. Example of Discretized Impedance Optimization

A. Design Goals and Optimization Results

We target to find designs of anomalous reflecting metasurfaces to realize the application scenario of Fig. 1 at three potential operational frequencies for D-band communications: $f_0 = [144.75; 157.75; 170.90]$ GHz (the corresponding operational wavelengths $\lambda_0 = [2.0725; 1.9017; 1.7554]$ mm), marked as Designs 1–3 in Table I). The incident TE-polarized plane wave comes from the normal direction $\theta_{\text{i}} = 0°$, and the goal is to reflect it into the oblique direction $\theta_{\text{r}} = 50°$. Thus, the metasurface period is $D = \lambda_0/\sin\theta_{\text{r}}$. We discretize the impedance sheet into $K = 8$ elements, and assume a quartz substrate with the permittivity $\epsilon_{\text{d}} = 4.2(1 - j0.005)$ and thickness $d = 209$ μm. In the optimization of the sheet reactances of the elements according to the cost function (12), the allowed solutions of Z_k were restricted to the range $[-2000j, +50j]$ Ohm. This constraint is introduced to make the actual implementations of the array elements easier, because large negative or positive reactances require some extreme geometries of metal elements that may be difficult or impossible to fabricate.

As a result of numerical optimization, we get a set of different solutions minimizing (12). From them, we select the most suitable one with reasonably decaying amplitudes of the evanescent surface wave harmonics, because high amplitudes of reactive fields near the array lead to smaller frequency bandwidth and higher losses. Fig. 3 shows an example of optimized mode amplitudes for the model of an infinite periodic structure. It is shown that the incident power is fully reflected to the anomalous direction ($n = 1$) with nearly zero specular reflection and $n = -1$ order reflection. The values of the discretized grid reactances are given in Table I as Z_{1-8} for the corresponding design frequencies.

Finally, we make full-wave simulations with Ansys HFSS to validate the structure performance on the level of the impedance sheet model, studying a supercell with Z_{k} consisting of eight elements at the grounded dielectric layer. The structure is simulated as an infinite array along x and y with the periodic boundary conditions under TE illumination realized with a Floquet port excitation. Knowledge of the magnitudes of the Floquet harmonics for a given periodicity along x found in simulations allows us to estimate the macroscopic reflection coefficient of the infinite structure [21], [22] and calculate the far-zone field reflected from a

TABLE I

Design Parameters of the Implemented Anomalous Reflectors. In Case of the Absence of an Element in the Subcell, the Dog-Bone Element Parameter Is Marked as "x"

	1	2	3
f_0, GHz	144.75	157.75	170.90
Z_1, Ohm	$-319j$	$-137j$	$-1229j$
Z_2, Ohm	$-1686j$	$-1010j$	$43j$
Z_3, Ohm	$-346j$	$-876j$	$-1074j$
Z_4, Ohm	$-138j$	$43j$	$-926j$
Z_5, Ohm	$-991j$	$-833j$	$-1250j$
Z_6, Ohm	$-1721j$	$-582j$	$-2000j$
Z_7, Ohm	$50j$	$-775j$	$-141j$
Z_8, Ohm	$-1140j$	$-1053j$	$-2000j$
C_{x1}, μm	156	181.7	50
C_{x2}, μm	64	82	0
C_{x3}, μm	205	60	65
C_{x4}, μm	286.5	0	125
C_{x5}, μm	119.5	55	155
C_{x6}, μm	63.7	152	x
C_{x7}, μm	0	150	201.7
C_{x8}, μm	98	140	x
C_{y1}, μm	40	40	40
C_{y2}, μm	40	40	0
C_{y3}, μm	40	40	40
C_{y4}, μm	40	0	40
C_{y5}, μm	40	40	40
C_{y6}, μm	40	40	x
C_{y7}, μm	0	40	40
C_{y8}, μm	40	40	x
L_{x1}, μm	60	60	60
L_{x2}, μm	60	60	116.4
L_{x3}, μm	60	60	60
L_{x4}, μm	60	145	60
L_{x5}, μm	60	60	60
L_{x6}, μm	60	60	x
L_{x7}, μm	98	60	60
L_{x8}, μm	60	60	x
L_{y1}, μm	100	100	40
L_{y2}, μm	60	60	$\lambda_0/10$
L_{y3}, μm	100	60	40
L_{y4}, μm	100	$\lambda_0/10$	40
L_{y5}, μm	60	60	40
L_{y6}, μm	60	60	x
L_{y7}, μm	$\lambda_0/10$	60	80
L_{y8}, μm	60	60	x
$\eta_{\text{eff}}^{\text{sim,LL}}$, %	99.72	98.65	97.33
$\eta_{\text{eff}}^{\text{sim,Lossy}}$, %	90.78	91.81	90.76

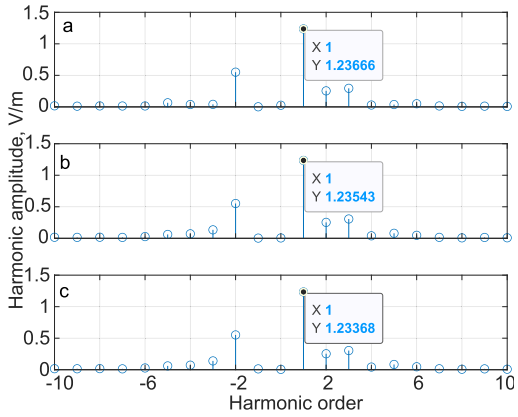

Fig. 3. Amplitudes of scattered harmonics for designed metasurfaces with optimized step-wise uniform sheets. (a) Design 1. (b) Design 2. (c) Design 3.

finite-size metasurface, whereas the reflection angle is defined in accordance with the model of diffraction on infinite periodic structures (2). Typically, the best numerically optimized solutions can realize the desired anomalous reflection with the efficiency at the level of 99.99%, if material losses are neglected.

The nonlocal and local (phase gradient) design approaches were compared for an example of reflection of normally incident waves to 50° in our recent paper [23]. The structures' performance was compared using full-wave simulations of the corresponding penetrable impedance sheet models. The results show that, for such moderate angle of anomalous reflection, both structures demonstrate high anomalous reflection efficiency, as expected from earlier works, for example, [6], [7], and [12]. On the other hand, nonlocal designs demonstrate significantly better performance for larger deviations from the specular reflection law, see [24] and an example in Section V.

B. Implementation of Elements in the Supercell

Our next goal is to find proper geometries of the metallic subcells that would realize the desired grid impedances Z_k. The grid impedance of a metallic patch or strip positioned on a grounded substrate can be determined using the circuit model [25]. To do that, we use the locally periodic approximation and simulate a single subcell using periodic boundary conditions in both x- and y-directions along the metasurface plane and find the reflection coefficient. The grid impedance of the meta-atom can be determined from the reflection coefficients and the substrate parameters. The incident angle in the simulation is defined as θ_i. The input impedance of the structure can be expressed in terms of the simulated reflection coefficient R as follows:

$$Z_\mathrm{in} = \frac{1+R}{1-R}\eta_0 \tag{13}$$

where $\eta_0 = \sqrt{\mu_0/\epsilon_0}$ is the free-space impedance, μ_0 and ϵ_0 are the permeability and permittivity of free space, respectively [25], [26], [27]. Z_in is the input impedance of the parallel connection of the grid impedance Z_g and the grounded substrate impedance Z_gd. Next, we extract the grid impedance using

$$Z_\mathrm{g} = \frac{Z_\mathrm{in}Z_\mathrm{gd}}{Z_\mathrm{gd}-Z_\mathrm{in}} \tag{14}$$

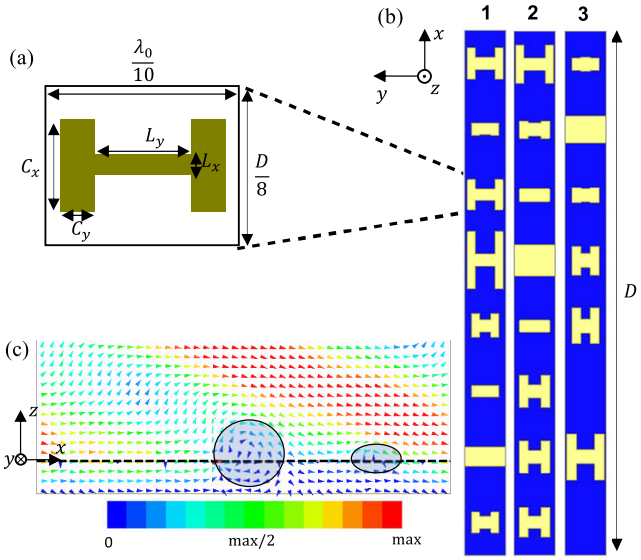

Fig. 4. Geometry of the implemented metasurface. (a) Subcell with parameters varied in the impedance extraction. (b) Final supercells implemented for three targeted designs of perfect anomalous reflectors. (c) Poynting vector distribution at the zx-plane. The shaded circle regions show the regions of nonlocal power exchange between free space and the metasurface volume.

where $Z_\mathrm{gd} = j\eta_\mathrm{d}\tan k_\mathrm{d}d$ and $k_\mathrm{d} = k_0\sqrt{\epsilon_\mathrm{d}-\sin^2\theta_\mathrm{i}}$ is the propagation constant in the dielectric substrate with $\eta_\mathrm{d} = \eta_0/\sqrt{\epsilon_\mathrm{d}-\sin^2\theta_\mathrm{i}}$ (for TE-polarized wave) and the free-space wavenumber $k_0 = \omega\sqrt{\epsilon_0\mu_0}$ [26].

The simplest geometry of capacitive subcells is a rectangular patch, but such elements exhibit very different responses for oblique and normal incidences. This strong angular dependence leads to some impedance mismatch when the elements are implemented in the final supercell, therefore requiring an additional global optimization of the whole supercell. For this reason, we used the so-called *dog-bone* geometry for the subcell metal pattern, illustrated in Fig. 4(a). This is one example of self-resonant grids [28] that are known to offer high angular stability of response from high-impedance surfaces, for example, [29], [30] and [31]. Varying the element's dimensions, we obtain corresponding parameters of the subcell to realize the required impedance values. Results for the extracted reactance Z_g for different structural parameters for Design 1 are presented in Fig. 5. It is worth noting a very high level of angular stability comparing the results for the normal and oblique incidences. The obtained values of the implemented elements' parameters are presented in Table I, and the top view of the implemented supercells is shown in Fig. 4(b). Some of the elements require rather large negative values of reactance, and our analysis shows that these elements can be substituted with simply open subcells without any element presented. Some other elements require a small positive reactance, which is implemented as inductive strips with the width L_x, that is, the length is equal to the overall y periodicity of the metasurface $L_y = \lambda_0/10$.

The final structures are simulated as infinite periodic structures. The results of simulations in the absence and presence of material losses are given in Table I as $\eta_\mathrm{eff}^\mathrm{sim,LL}$ (with lossless metal) and $\eta_\mathrm{eff}^\mathrm{sim,Lossy}$ (with gold layers of 200 nm thickness), respectively. The results show that the reflection efficiency

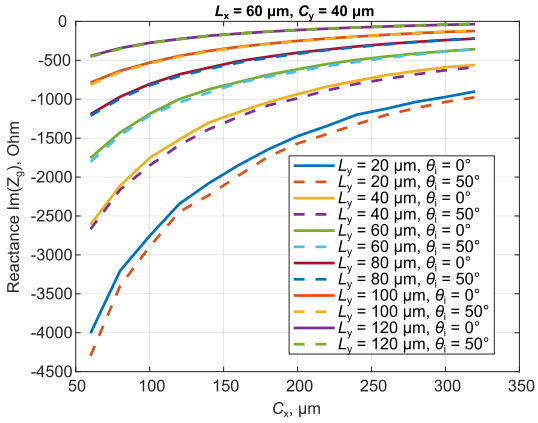

Fig. 5. Extracted impedance values and the angular stability analysis.

slightly (∼1%–3%) degrades after the implementation of a realistic structure, in comparison with the performance of the optimized sheet-impedance model. When metal losses are taken into account, the efficiency degrades toward ∼ 90%, mainly due to excited nonpropagating surface waves along the metasurface. The efficiency can be improved if the metal deposition thickness increases (reducing the Ohmic loss in metal).

Fig. 4(c) shows the simulated Poynting vector distribution of Design 1 in the xoz-plane. It is clear that in the regions marked by shaded circles, there is nonlocal power exchange between the metasurface volume and free space. The power flows into the metasurface (virtual loss) and then it is re-radiated into free space (virtual gain). For the other two implemented designs, we see a qualitatively similar picture showing nonlocality of power reflection. Note that although the given examples show nonlocal reflection and only global power conservation, the developed design method is general and can find both local and nonlocal solutions.

IV. Experimental Validation

In order to fabricate the designed anomalous reflectors, we used a standard cleanroom photolithography manufacturing process, with 4-in quartz wafers for the substrate. In [23], theoretical estimations of the link budget for NLOS D-band communication scenarios are presented and compared with other existing models. The choice of the waver size was made based on these theoretical estimations. These estimations show that this size is enough to ensure reliable indoor communications. We used AZ514E photoresist, 5 nm Ti and 200 nm Au for both the front side patterning and the ground plane. This Au layer thickness was selected in order to reasonably minimize the resistive losses, as they may significantly affect the device performance.

For experimental validation, we follow a similar procedure as presented in [27]. A quasi-optical set-up is used for collimation of the incident illumination from the horn antenna into a narrow spot on the metasurface sample under study. This allows us to effectively measure the macroscopic reflection coefficient as a parameter describing response from the corresponding infinite structure, avoiding the effects of scattering by the edges.

The experimental set-up is shown in Fig. 6(a). The used vector network analyzer (VNA) is Keysight PNA Network Analyzer N5225A (10 MHz–50 GHz) with WR 5.1 VDI extension units operating at 140–220 GHz. A WR-5 rectangular horn antenna Elmika RHA-015E with 22 dBi directivity was used as the source antenna. The set-up contains three 90° parabolic mirrors M1, M2, and M3 with the corresponding focal distances $F_1 = 2.54$ cm, $F_2 = 15.24$ cm, and $F_3 = 12.7$ cm. Note that, the characterization of anomalous reflector usually needs two-port measurement system, that is, two horn antennas are required in the normal and anomalous directions. Here, we use quasi-optical measurement system and time-gating method to simplify it as one-port system. The Gaussian beam emitted from the source Horn antenna is collimated by mirror M1 and converged by M2 toward the normal of sample. The beam is then reflected to the anomalous direction by the sample. Finally, the beam is reflected by flat mirror M4 and goes back to the horn antenna along the same route. The efficiency of anomalous reflection is determined by measuring the reflection coefficient S_{11}. Note that in this method, the beam is reflected twice by the sample. Also, the spurious reflections from all the mirrors can be corrected by normalization. The normalization is made by measuring the reflection coefficient when the sample is replaced by a flat mirror rotated to $\theta_r/2 = 25°$. In order to estimate the retroreflection level for the normal incidence, we measured the intensity of the reflected signal tuning the time-gating parameters for reflection from the sample. Another anomalously reflected harmonic ($n = -1$) was measured by upturning the sample. The last measurement is approximate, due to the fact that the measured area could not be exactly at the same position as the originally measured for the desired anomalously reflected mode.

The experimental results are presented in Fig. 7. Here, the shown data point gives the efficiency measured at the targeted design frequency. These results are in good agreement with the theoretically and numerically estimated values presented in Table I. For all three design cases, one can estimate the operational band of effective anomalous reflection. As a practically acceptable level, we define a region where the measured anomalous reflection efficiency is above 50%. Due to the frequency limit of the used extender (140 GHz), we could not observe the whole operational bands for Designs 1 and 2, therefore the lower limit of the operational band in these cases is in fact wider than defined on the experimentally validated data. Design 1 provides more than half-power anomalous reflection efficiency in the range 140–157.4 GHz; Design 2 grants it in the range 140–170 GHz; and Design 3 covers the range 140.6–183.1 GHz.

V. Anomalous Reflector for 70° Tilt of the Reflected Beam

The presented design method is general and can be used, for example, for designing anomalous reflectors with arbitrary deflection angles without parasitic reflections. In order to demonstrate the universality of the design method, we provide in this section a comparative analysis of anomalous reflectors

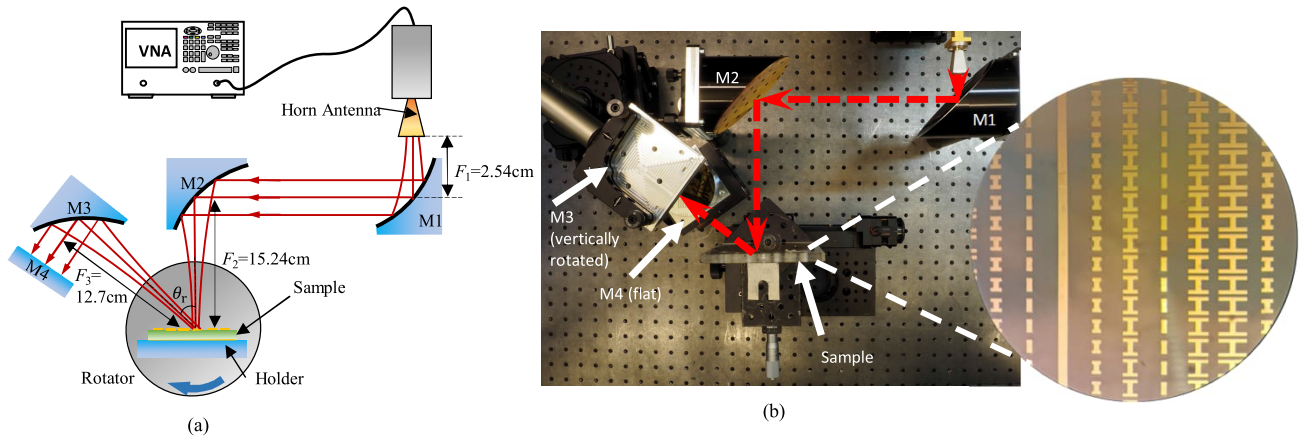

Fig. 6. (a) Schematics and (b) photograph of the experimental setup and structure details of Design 1 under microscope.

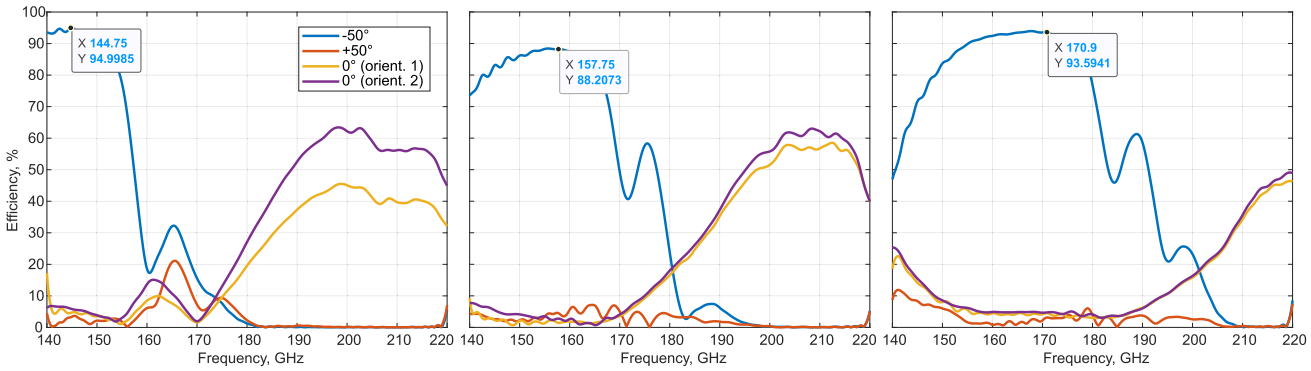

Fig. 7. Reflection efficiency measured with the quasi-optical method. The curve markers indicate the corresponding design frequency (X) and the measured efficiency level (Y). Curve marked "−50°" corresponds to the desired anomalously reflected mode $n = -1$; Curve "+50°" is for the same mode measured after flipping the sample; "0° (orient. 1)" curve shows the retroreflection level for the normal incidence corresponding to the orientation of the sample applied while measuring the case with "−50°" and "0° (orient. 1)" corresponds to the same case, but for +50°.

designed for $\theta_i = 0°$ and $\theta_r = 70°$ using nonlocal and phase-gradient methods. We validate the structure performance via full-wave simulations of infinite structures using the model of a penetrable impedance sheet at a lossy substrate backed by a metal ground plane with a finite conductivity. As an example, we consider the operational frequency of 144.75 GHz. In order to realize reflection to 70° at this frequency, the period of the structure is modified accordingly, as dictated by (2).

For the phase-gradient approach, the discretized values of the required sheet impedance for $\theta_i = 70°$ and $\theta_r = 0°$ (the reciprocal scenario of anomalous reflection into $n = -1$ harmonic) read $Z_{1-8} = [-552.86, -447.49, -334.83, -161.52, 340.73, -3706, -978.71, -690.76]j$ Ohm. Implementing the dog-bone meta-atom elements similar to the procedure discussed in Section III-B and considering both dielectric and metal losses, we get from the EM simulation of an infinite structure the anomalous reflection efficiency $\eta_{\text{eff}} = 0.7142$.

Using the nonlocal design method presented here, we find the required reactive sheet impedance values as $Z_{1-8} = [-132, -278, -187, -1215, -1099, -1008, -989, 50]j$ Ohm. EM simulation of the infinite structure with implemented dog-bone elements considering all the material losses shows the efficiency of the anomalous reflector $\eta_{\text{eff}} = 0.8930$. This example demonstrates strong benefits of the nonlocal design compared to the phase-gradient approach in case of significant deviations from the usual reflection law.

VI. Conclusion

As one of the first steps toward realization of efficient control of wave reflections in D-band communication scenarios, we have presented a method for the design and implementation of metasurfaces with advanced functionalities based on optimizations of discretized sheet impedance profiles. As an example, we have experimentally confirmed functionality of a designed and manufactured D-band anomalous reflector. The developed fast numerical optimization approach allows us to directly find useful solutions without the need of further discretization or detailed numerical tuning of the geometry of the array subcells. The considered example of practical implementation was targeted for a 50° anomalous reflector operating in D-band, which is one of the first realizations of anomalous reflectors in this frequency range. It is worth noting that the proposed method is general and not limited to the considered scenario of anomalous reflection. The method can be directly applied to the design of various beam-shaping surfaces, splitters with phase control of all beams, and other metasurface devices, just by modifying the optimization objective function (see our recent research in [32]).

Furthermore, the developed discrete-impedance metasurface design method can be potentially used also in the design of reconfigurable reflectors. This can be explained as follows. By integrating reconfigurable elements into each meta-atom (subcell), it is possible to control the sheet impedance of each subcell independently. In practice, the subcell size remains fixed. However, the size of the supercell (the metasurface period) can be modified discretely by increasing or decreasing the number of small subcells forming one supercell. Reconfigurability can be provided by integrating tunable elements, for example, varactors or mems capacitors, in metallic structures [33]. Assuming that one supercell contains K subcells of the size d_{sub}, the anomalous reflection angle can be found from relation $\sin\theta_{\text{r}} = \lambda/D = \lambda/(Kd_{\text{sub}})$ if $\theta_{\text{i}} = 0$ [see (2)]. Thus, by increasing or decreasing the number of subcells whose impedances are set to form one period, the anomalous reflection angle can be discretely tuned. If d_{sub} is enough small, the neighboring discrete angles of θ_{r} are closely spaced, emulating a continuous sweeping of reflected beams. It is important to note that such functionality cannot be realized by periodic metagratings with sparse elements. Although it was recently demonstrated that nonperiodic metagratings can achieve dynamic scanning by globally optimizing all meta-atoms [34], our approach only needs an optimization of meta-atoms in one supercell, which significantly improves the optimization efficiency. Thus, we consider this method suitable for the development of not only static reflection-control surfaces but also for future reconfigurable intelligent surfaces.

Appendix

Here, we show derivations of (8) and (9). The total tangential electric and magnetic fields are the sum of tangential incident and reflected fields on the metasurface plane ($z = 0$)

$$\mathbf{E}_{\text{tot}} = \mathbf{E}_{\text{i}} + \mathbf{E}_{\text{r}} \tag{15}$$

and

$$\mathbf{H}_{\text{tot}} = \mathbf{H}_{\text{i}} + \mathbf{H}_{\text{r}}. \tag{16}$$

Assuming a TE-polarized wave incident on the metasurface, the tangential magnetic field is related with electric field by the free-space wave admittance matrix

$$\hat{z} \times \mathbf{H}_{\text{i}} = \mathbf{Y}_0 \cdot \mathbf{E}_{\text{i}}, \quad \hat{z} \times \mathbf{H}_{\text{r}} = -\mathbf{Y}_0 \cdot \mathbf{E}_{\text{r}}. \tag{17}$$

Note that the tangential magnetic field flips its sign after reflection, orienting along $-x$-direction, as shown in Fig. 8(a). The total tangential fields are related by the impedance boundary condition

$$\mathbf{Y}_{\text{tot}} \cdot \mathbf{E}_{\text{tot}} = \hat{z} \times \mathbf{H}_{\text{tot}}. \tag{18}$$

Substituting (15)–(17) into (18), we can obtain the relation between the incident and reflected electric fields

$$\mathbf{E}_{\text{r}} = (\mathbf{Y}_{\text{tot}} + \mathbf{Y}_0)^{-1} \cdot (\mathbf{Y}_0 - \mathbf{Y}_{\text{tot}}) \cdot \mathbf{E}_{\text{i}} = \mathbf{\Gamma}_{\text{TE}} \cdot \mathbf{E}_{\text{i}}. \tag{19}$$

For the TM polarization, we define the reflection matrix in terms of tangential magnetic fields $\mathbf{H}_{\text{r}} = \mathbf{\Gamma}_{\text{TM}} \cdot \mathbf{H}_{\text{i}}$. In this case, it is more convenient to relate the tangential electric and magnetic fields via the wave impedance as follows:

$$\mathbf{E}_{\text{i}} = \mathbf{Z}_0 \cdot (\hat{z} \times \mathbf{H}_{\text{i}}), \quad \mathbf{E}_{\text{r}} = -\mathbf{Z}_0 \cdot (\hat{z} \times \mathbf{H}_{\text{r}}). \tag{20}$$

Substituting (15), (16), and (20) into (18), we obtain

$$\mathbf{H}_{\text{r}} = (\mathbf{Z}_{\text{tot}} + \mathbf{Z}_0)^{-1} \cdot (\mathbf{Z}_0 - \mathbf{Z}_{\text{tot}}) \cdot \mathbf{H}_{\text{i}} = \mathbf{\Gamma}_{\text{TM}} \cdot \mathbf{H}_{\text{i}}. \tag{21}$$

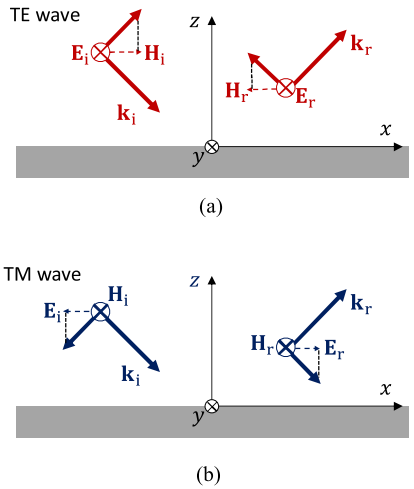

Fig. 8. Definitions of the coordinate system and field orientations for (a) TE- and (b) TM-polarized waves.

Acknowledgment

The authors acknowledge the use of facilities of Aalto University at OtaNano—Micronova Nanofabrication Center. They would like to thank Prof. Sami Franssila, Dr. Ville Jokinen, Dr. Victor Ovchinnikov, Dr. Mikhail Omelyanovich, Dr. Andrey Generalov, Dr. Irina Nefedova, and Mr. Pouyan Rezapoor for their useful comments and discussions related to microfabrication and mm-wave measurement issues.

References

[1] D. Berry, R. Malech, and W. Kennedy, "The reflectarray antenna," *IEEE Trans. Antennas Propag.*, vol. AP-11, no. 6, pp. 645–651, Nov. 1963.

[2] J. Huang and J. A. Encinar, *Reflectarray Antennas*. Hoboken, NJ, USA: Wiley, 2008.

[3] D. M. Pozar, "Wideband reflectarrays using artificial impedance surfaces," *Electron Lett.*, vol. 43, no. 3, pp. 148–149, Feb. 2007.

[4] N. Yu et al., "Light propagation with phase discontinuities: Generalized laws of reflection and refraction," *Science*, vol. 334, no. 6054, pp. 333–337, Oct. 2011.

[5] N. M. Estakhri and A. Alù, "Wave-front transformation with gradient metasurfaces," *Phys. Rev. X*, vol. 6, no. 4, Oct. 2016, Art. no. 041008.

[6] V. S. Asadchy, M. Albooyeh, S. N. Tcvetkova, A. Díaz-Rubio, Y. Ra'di, and S. A. Tretyakov, "Perfect control of reflection and refraction using spatially dispersive metasurfaces," *Phys. Rev. B, Condens. Matter*, vol. 94, no. 7, Aug. 2016, Art. no. 075142.

[7] A. Epstein and G. V. Eleftheriades, "Synthesis of passive lossless metasurfaces using auxiliary fields for reflectionless beam splitting and perfect reflection," *Phys. Rev. Lett.*, vol. 117, no. 25, Dec. 2016, Art. no. 256103.

[8] D.-H. Kwon, "Lossless scalar metasurfaces for anomalous reflection based on efficient surface field optimization," *IEEE Antennas Wireless Propag. Lett.*, vol. 17, no. 7, pp. 1149–1152, Jul. 2018.

[9] J. Budhu and A. Grbic, "Perfectly reflecting metasurface reflectarrays: Mutual coupling modeling between unique elements through homogenization," *IEEE Trans. Antennas Propag.*, vol. 69, no. 1, pp. 122–134, Jan. 2021.

[10] A. Díaz-Rubio, V. S. Asadchy, A. Elsakka, and S. A. Tretyakov, "From the generalized reflection law to the realization of perfect anomalous reflectors," *Sci. Adv.*, vol. 3, no. 8, Aug. 2017.

[11] T. He et al., "Perfect anomalous reflectors at optical frequencies," *Sci. Adv.*, vol. 8, no. 9, Mar. 2022, Art. no. eabk3381.

[12] V. S. Asadchy, A. Wickberg, A. Díaz-Rubio, and M. Wegener, "Eliminating scattering loss in anomalously reflecting optical metasurfaces," *ACS Photon.*, vol. 4, no. 5, pp. 1264–1270, May 2017.

[13] Y. Kato, K. Omori, and A. Sanada, "D-band perfect anomalous reflectors for 6G applications," *IEEE Access*, vol. 9, pp. 157512–157521, 2021.

[14] Y. Ra'di, D. L. Sounas, and A. Alù, "Metagratings: Beyond the limits of graded metasurfaces for wave front control," *Phys. Rev. Lett.*, vol. 119, no. 6, Aug. 2017, Art. no. 067404.

[15] O. Rabinovich and A. Epstein, "Analytical design of printed circuit board (PCB) metagratings for perfect anomalous reflection," *IEEE Trans. Antennas Propag.*, vol. 66, no. 8, pp. 4086–4095, Aug. 2018.

[16] X. Wang, A. Díaz-Rubio, H. Li, S. A. Tretyakov, and A. Alù, "Theory and design of multifunctional space-time metasurfaces," *Phys. Rev. Appl.*, vol. 13, no. 4, Apr. 2020, Art. no. 044040.

[17] X. Wang, A. Díaz-Rubio, and S. A. Tretyakov, "Independent control of multiple channels in metasurface devices," *Phys. Rev. Appl.*, vol. 14, no. 2, Aug. 2020, Art. no. 024089.

[18] M. T. Ivrlac and J. A. Nossek, "Toward a circuit theory of communication," *IEEE Trans. Circuits Syst. I, Reg. Papers*, vol. 57, no. 7, pp. 1663–1683, Jul. 2010.

[19] R. Faqiri, C. Saigre-Tardif, G. C. Alexandropoulos, N. Shlezinger, M. F. Imani, and P. del Hougne, "PhysFad: Physics-based end-to-end channel modeling of RIS-parametrized environments with adjustable fading," *IEEE Trans. Wireless Commun.*, vol. 22, no. 1, pp. 580–595, Jan. 2023.

[20] C. Kohlberger and A. Stelzer, "Multi-modal scattering and propagation through several close periodic grids," *IEEE Trans. Antennas Propag.*, vol. 70, no. 7, pp. 5758–5769, Jul. 2022.

[21] A. Díaz-Rubio and S. A. Tretyakov, "Macroscopic modeling of anomalously reflecting metasurfaces: Angular response and far-field scattering," *IEEE Trans. Antennas Propag.*, vol. 69, no. 10, pp. 6560–6571, Oct. 2021.

[22] A. Díaz-Rubio, S. Kosulnikov, and S. A. Tretyakov, "On the integration of reconfigurable intelligent surfaces in real-world environments: A convenient approach for estimation reflection and transmission," *IEEE Antennas Propag. Mag.*, vol. 64, no. 4, pp. 85–95, Aug. 2022.

[23] S. Kosulnikov, F. S. Cuesta, X. Wang, and S. A. Tretyakov, "Simple link-budget estimation formulas for channels including anomalous reflectors," *IEEE Trans. Antennas Propag.*, vol. 71, no. 6, pp. 5276–5288, Jun. 2023.

[24] M. Movahediqomi, G. Ptitcyn, and S. Tretyakov, "Comparison between different designs and realizations of anomalous reflectors for extreme deflections," *IEEE Trans. Antennas Propag.*, vol. 71, no. 10, pp. 8007–8017, Oct. 2023.

[25] X.-C. Wang et al., "Systematic design of printable metasurfaces: Validation through reverse-offset printed millimeter-wave absorbers," *IEEE Trans. Antennas Propag.*, vol. 66, no. 3, pp. 1340–1351, Mar. 2018.

[26] D. M. Pozar, *Microwave Engineering*, 4th ed. Hoboken, NJ, USA: Wiley, 2012.

[27] X. Wang et al., "Extreme asymmetry in metasurfaces via evanescent fields engineering: Angular-asymmetric absorption," *Phys. Rev. Lett.*, vol. 121, no. 25, Dec. 2018, Art. no. 256802.

[28] I. Anderson, "On the theory of self-resonant grids," *Bell Syst. Tech. J.*, vol. 54, no. 10, pp. 1725–1731, Dec. 1975.

[29] C. R. Simovski, P. de Maagt, and I. V. Melchakova, "High-impedance surfaces having stable resonance with respect to polarization and incidence angle," *IEEE Trans. Antennas Propag.*, vol. 53, no. 3, pp. 908–914, Mar. 2005.

[30] A. Vallecchi and A. G. Schuchinsky, "Entwined planar spirals for artificial surfaces," *IEEE Antennas Wireless Propag. Lett.*, vol. 9, pp. 994–997, 2010.

[31] J. Shabanpour and C. R. Simovski, "Angular and polarization stability of broadband reconfigurable intelligent surfaces of binary type," *IEEE Access*, vol. 10, pp. 126253–126268, 2022.

[32] S. Kosulnikov, F. S. Cuesta, X. Wang, and S. A. Tretyakov, "Molding of reflection and scattering from uniform walls using space-periodic metasurfaces," 2023, *arXiv:2306.09250*.

[33] M. A. ElMossallamy, H. Zhang, L. Song, K. G. Seddik, Z. Han, and G. Y. Li, "Reconfigurable intelligent surfaces for wireless communications: Principles, challenges, and opportunities," *IEEE Trans. Cognit. Commun. Netw.*, vol. 6, no. 3, pp. 990–1002, Sep. 2020.

[34] V. Popov, B. Ratni, S. N. Burokur, and F. Boust, "Non-local reconfigurable sparse metasurface: Efficient near-field and far-field wavefront manipulations," *Adv. Opt. Mater.*, vol. 9, no. 4, Feb. 2021, Art. no. 2001316.